Nanoscale

PAPER

Cite this: *Nanoscale*, 2018, **10**, 14165

T-Nb$_2$O$_5$ nanoparticle enabled pseudocapacitance with fast Li-ion intercalation†

Lingping Kong,[a] Xiaoteng Liu,[b] Jinjia Wei,[a] Steven Wang,[c] Ben Bin Xu, *[b] Donghui Long *[d] and Fei Chen*[a,b]

Received 29th April 2018,
Accepted 27th June 2018

DOI: 10.1039/c8nr03495h

rsc.li/nanoscale

Orthorhombic Nb$_2$O$_5$ (T-Nb$_2$O$_5$) nanocrystallites are successfully fabricated through an evaporation induced self-assembly (EISA) method guided by a commercialised triblock copolymer – Pluronic F127. We demonstrate a morphology transition of T-Nb$_2$O$_5$ from continuous porous nanofilms to monodisperse nanoparticles by changing the content of Pluronic F127. The electrochemical results show that the optimized monodisperse Nb-2 with a particle size of 20 nm achieves premier Li-ion intercalation kinetics and higher rate capability than mesoporous T-Nb$_2$O$_5$ nanofilms. Nb-2 presents an initial intercalation capacity of 528 and 451 C g^{-1} at current densities of 0.5 and 5 A g^{-1} and exhibited a stable capacity of 499 C g^{-1} after 300 charge/discharge cycles and 380 C g^{-1} after 1000 cycles, respectively. We would expect this copolymer guided monodispersion of T-Nb$_2$O$_5$ nanoparticles with high Li$^+$ intercalation performance to open up a new window for novel EES technologies.

Introduction

Recently, the research on high performance electrochemical energy storage (EES) has made significant progress by innovating pseudocapacitive materials, *i.e.* transition metal oxides.[1–4] Faradaic charge storage in transition metal oxides enables high power density and high energy density through a fast sequence of reversible faradaic redox, electrosorption or intercalation processes at the surface or near-surface region of electrodes.[5,6] Unlike traditional battery materials, the charge/discharge processes in pseudocapacitors are not dominated by ion diffusion, thus, charge storage can occur on the order of seconds and minutes. The latest research trend in high performance pseudocapacitive materials is to design novel materials with a short path length and high active-surface area by controlling the nano-morphologies.[7–13]

Orthorhombic Nb$_2$O$_5$ (T-Nb$_2$O$_5$), a typical pseudocapacitive material, holds a unique property of reversible Li-ion intercalation reaction, $\mathrm{Nb_2O_5} + x\mathrm{Li}^+ + xe^- \leftrightarrow \mathrm{Li}_x\mathrm{Nb_2O_5}$, where a maximum capacity of charge storage can be reached at 728 C g^{-1} when x is 2.[3] T-Nb$_2$O$_5$ has attracted considerable interest for its high theoretical specific capacity, fast Li-ion intercalation kinetics and reversible lithiation/delithiation processes.[14–18] Some strategies have been proposed to synthesise Nb$_2$O$_5$ with desired morphologies, aiming to optimise the electrochemical properties.[19–23] Brezesinski *et al.* synthesized ordered mesoporous T-Nb$_2$O$_5$ thin films and achieved significant enhancement in capacitive energy storage.[24] Liu and his co-workers fabricated Nb$_2$O$_5$ nanosheets through hydrothermal reactions and obtained high rate Li-ion storage performance with the Nb$_2$O$_5$ nanosheets.[25] Zhou *et al.* used Nb$_2$O$_5$ nanobelts as a lithium intercalation electrode which showed high reversible capacity, high rate capability and excellent cycling stability.[26]

The low dimensional T-Nb$_2$O$_5$ structure brings advantages that can facilitate electrolyte ions and electron transfer, offer a high surface area with abundant active sites and sustain the crystal structure for durable charge/discharge processes. However, developing a facile and sustainable method to prepare T-Nb$_2$O$_5$ nanocrystals, controllably forming the desired morphologies, and using it to improve the charge storage capacity for EES remain a challenge.

In this paper, we propose a facile process – evaporation induced self-assembly (EISA) guided by a triblock copolymer – Pluronic F127 (a.k.a F127), to fabricate a T-Nb$_2$O$_5$ nanostructure. Different crystallite sizes and morphologies can be achieved by tuning the weight ratio of F127 from 0.5 to 2; a phase transition from mesoporous nanofilms to monodisperse nanoparticles will be demonstrated. We also discover that the monodisperse T-Nb$_2$O$_5$ nanoparticles exhibited faster Li-ion

---

[a] *School of Chemical Engineering and Technology, Xi'an Jiaotong University, Xi'an 710049, China. E-mail: feichen@xjtu.edu.cn*
[b] *Smart Materials and Surfaces Laboratory, Faculty of Engineering and Environment, Northumbria University, Newcastle upon Tyne NE1 8ST, UK. E-mail: ben.xu@northumbria.ac.uk*
[c] *School of Chemical Engineering and Advanced Materials, Newcastle University, Newcastle Upon Tyne, Tyne and Wear NE1 7RU, UK*
[d] *State Key Laboratory of Chemical Engineering, East China University of Science and Technology, Shanghai 200237, China. E-mail: longdh@mail.ecust.edu.cn*

† Electronic supplementary information (ESI) available. See DOI: 10.1039/c8nr03495h

intercalation kinetics and higher rate capacity than continuous mesoporous *T*-Nb_2O_5 nanofilms with a similar crystallite size. This finding could bring a new concept for novel Nb_2O_5 electrodes with fast Li-ion intercalation by introducing monodisperse nanoparticles.

Results and discussion

Structural and morphological characterization

The schematic of the EISA process and structure measurement by XRD are presented in Fig. 1. The inorganic $NbCl_5$ and guiding agent F127 nucleation first reacted (Fig. 1a) to form O–Nb–O bridges, accompanied by an aqueous sol–gel process. An organic–inorganic hybrid structure was generated by the following aggregation of $NbCl_5$/F127 micelles. Finally, the amorphous Nb_2O_5 crystallites were transited into an orthorhombic structure when we annealed the Nb/F127 precursor films at 600 °C. The particle size and morphology of *T*-Nb_2O_5 can be directly regulated by controlling the amount of F127. The weight ratios of F127 to Nb_2O_5 were designed as 0.5 : 1, 1 : 1, 1.5 : 1 and 2 : 1, with the samples named Nb-0.5, Nb-1, Nb-1.5 and Nb-2, respectively.

The XRD results in Fig. 1b suggest high crystallinity with an orthorhombic unit cell, which can be indexed to the JCPDS No. 30-0873, *i.e.* the diffraction peaks centred at 22.6, 28.4, 36.6, 42.8, 45.0, 46.2, and 50.9° can be indexed to the (001), (180), (181), (2100), (2110), (002), and (380) reflections of *T*-Nb_2O_5, respectively. The XRD results also reveal a decrease of the average crystallite size due to the increase of F127, which agrees well with the predicted results obtained from Scherrer's equation (Table S1†). We use TGA and DSC to verify the component ratios of F127 to Nb_2O_5 in weight (Fig. S1†) and find that there is a slight weight loss from 50 to 200 °C due to the removal of residual water and solvent as well as the oxidation of some remaining organic groups. Between 200 °C and 350 °C, the F127 decomposes thoroughly. An exothermic peak appears beyond 400 °C, indicating the rearrangement of the crystal structure. The XPS spectrum of Nb-2 in Fig. S2† presents two peaks, $Nb3d_{5/2}$ at 207.00 eV and $Nb3d_{3/2}$ at 209.75 eV, which are in good agreement with the binding energies of Nb_2O_5.

The porosity properties of samples were assessed by N_2 adsorption–desorption isotherms; the pore size distribution data are shown in Fig. S3.† These isotherms present very similar type IV isotherms with a hysteresis loop at P/P_0 of 0.8–1, suggesting the coexistence of mesopores and macropores. With increasing the amount of F127, the specific surface area and the average mesoporous diameters are increased, which also lead to a more active edge surface. More porosity data are provided in Table S1.†

We next study the morphology of *T*-Nb_2O_5 as a function of the weight ratio of F127 to Nb_2O_5. SEM observations in Fig. 2a–2d revealed that the particle size decreases with the increasing amount of F127; the overall morphology is very different from that of Nb_2O_5 without F127 (Fig. S4†). By adding F127, the morphology starts with continuous mesoporous nanofilms (Nb-0.5, Nb-1, and Nb-1.5) and then transits into monodisperse nanoparticles (Nb-2). From the TEM images of Nb-0.5 (Fig. 2e) and Nb-2 (Fig. 2f), we find that Nb-2 has a smaller size of around 20 nm with a disordered particle-overlapped structure. The HR-TEM image in Fig. 2f (insert) unveils the (001) plane (lattice parameter of 3.90 Å) in the Nb-2 nanocrystals corresponding to the orthorhombic structure.

Electrochemical characterization

The cyclic voltammetry (CV) results at various sweep rates are presented in Fig. 3a–d. At a low sweep rate, all CVs show symmetric anodic and cathodic peaks with ignorable voltage separation. This means that fast and reversible Li-ion interactions occurred within *T*-Nb_2O_5 ($Nb_2O_5 + xLi^+ + xe^- = Li_xNb_2O_5$, $0 < x < 2$). Moreover, the Nb-1.5 and Nb-2 at 1 mV s^{-1} show two cathodic peaks at around 1.45 V and 1.75 V, respectively. However, Nb-0.5 and Nb-1 exhibit only one broad cathodic peak around 1.45 V. Our hypothesis is that additional intercalation active sites occur in Nb-1.5 and Nb-2, due to their

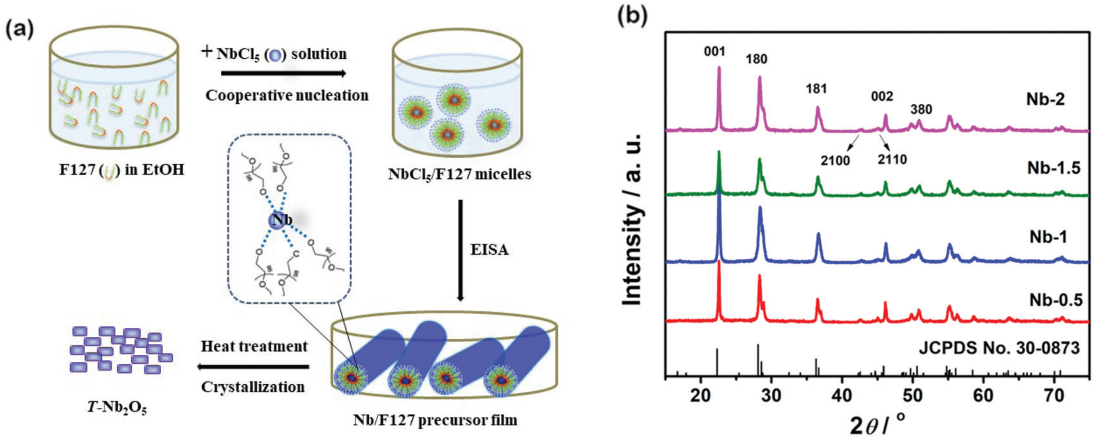

Fig. 1 (a) Schematic of the synthesis process and (b) XRD results for all samples.

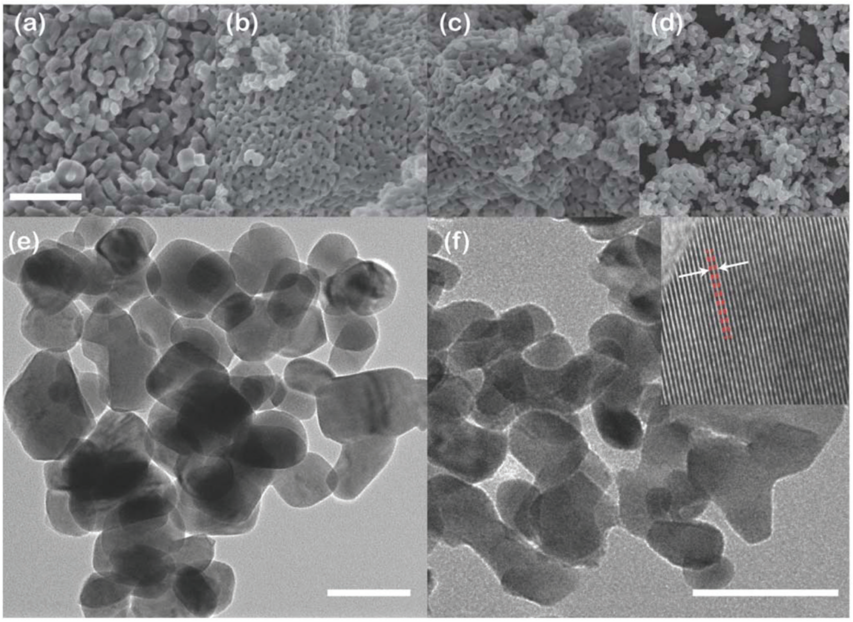

Fig. 2 SEM observations of (a) Nb-0.5, (b) Nb-1, (c) Nb-1.5 and (d) Nb-2; the scale bars are 500 nm; TEM results of (e) Nb-0.5 and (f) Nb-2; the scale bars are 50 nm.

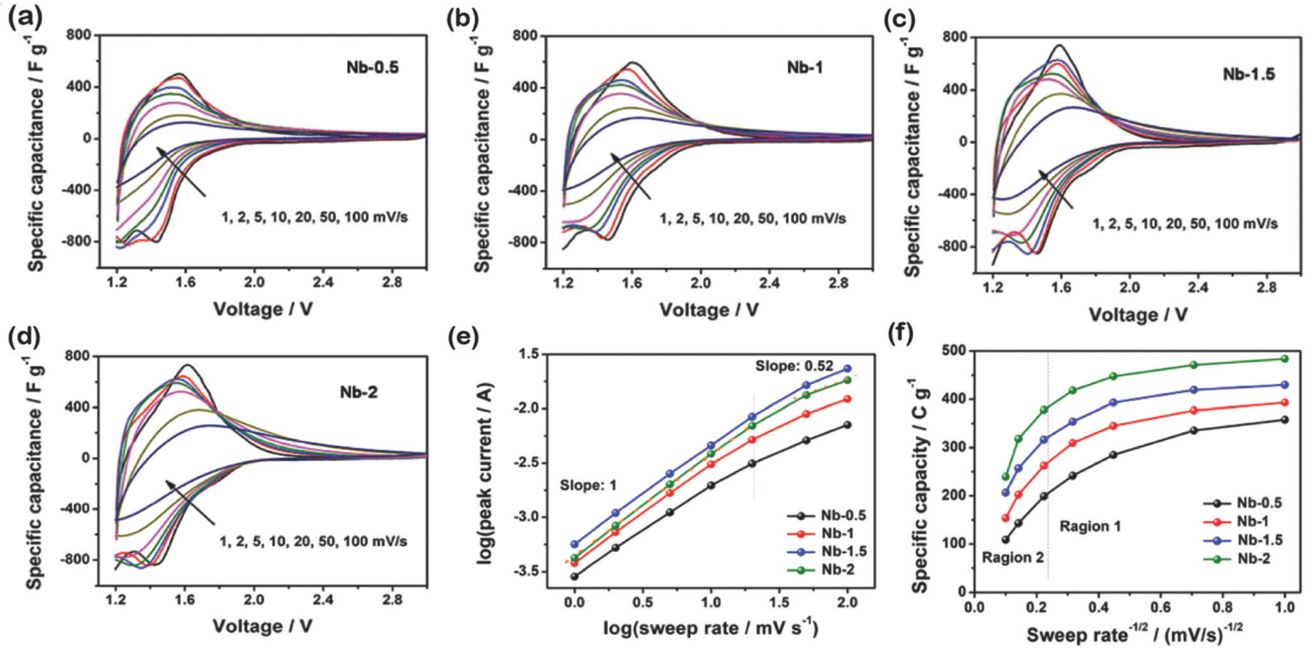

Fig. 3 CV curves of (a) Nb-0.5, (b) Nb-1, (c) Nb-1.5 and (d) Nb-2 at increasing scan rate at room temperature in a 3-limbed cell; (e) plot of specific capacity *vs.* $v^{-1/2}$ and (f) *b*-value determination of the peak cathodic currents. Electrochemical tests were performed at room temperature using a three-electrode system.

smaller crystalline size and more specific surface area that enable fast Li^+ transportation. Among all CV results, the potential region of 2–3 V makes minor contributions to the total capacity, while this region expands the operating potential window, thus greatly improving the total energy density according to the equation: $E = \frac{1}{2}C_S\Delta V^2$.

We next study the relationship between the capacity and sweep rate to further understand the Li-ion intercalation. The plots of specific capacity *vs.* $\nu^{-1/2}$ in Fig. 3f show two distinct regions. In region 1 (ν < 20 mV s^{-1}), the specific capacity is mostly independent of the sweep rate, which means that charge storage mainly arises from the capacitive process. In

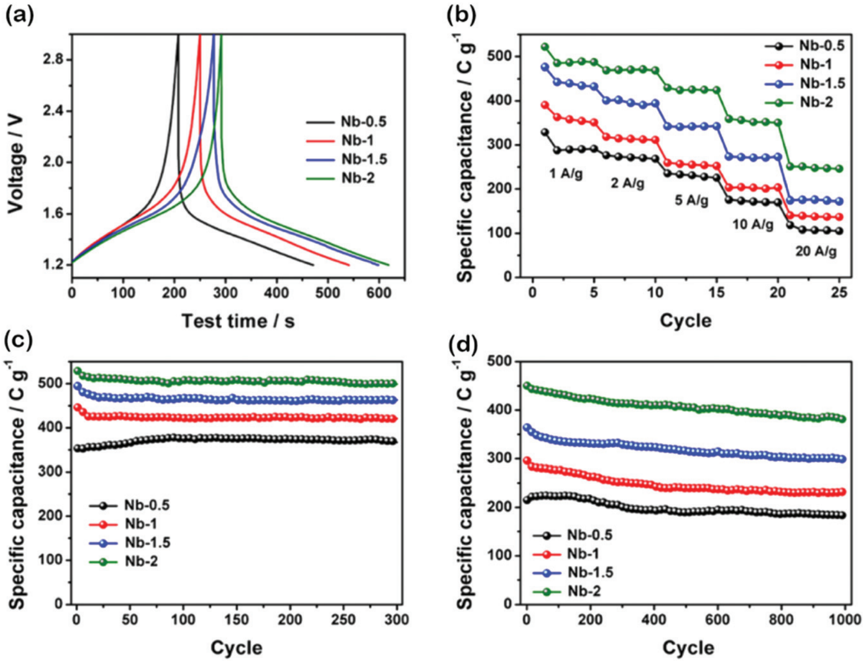

Fig. 4 (a) GCD curves, (b) rate capability and (c and d) cyclic performances for all samples.

region 2 (ν > 20 mV s^{-1}), the specific capacity decreases quickly with ν, indicating that charge storage is mainly controlled by the diffusion process. After comparing the galvanostatic charge–discharge (GCD) curves of all samples at a current density of 1 A g^{-1} (Fig. 4a), we discover that T-Nb$_2$O$_5$ undergoes a highly reversible Li$^+$ intercalation reaction by showing symmetric slope curves. The initial specific capacity of Nb-2 reaches the highest value as 521 C g^{-1} at 1 A g^{-1}. Nb-2 also has the best rate capability (Fig. 4b) with a slight decrease in the capacitance as the current density increases. At a high current density of 20 A g^{-1}, Nb-2 can still deliver a reasonably high capacity of 250 C g^{-1}. Moreover, the Nyquist plot of Nb-2 in Fig. S5† shows a high phase-angle impedance property and a low faradaic charge transfer resistance which accelerated the fast Li-ion intercalation.

The kinetic mechanism of the Li$^+$ insertion/extraction reaction was investigated from the relationship between the sweep rate and the capacity or current, which can be expressed as $i = a\nu^b$. When the value of b is 0.5, the current is controlled by the diffusion process. When b is 1, it means that the Li-ion intercalation process shows capacitive behaviour. By scaling log(i) *versus* log(ν) of cathodic peaks, the value of b can be calculated as shown in Fig. 3e. It is found that the b value for Nb-2 is 1 corresponding to a typical capacitive intercalation. We found that Nb-1.5 has a b-value of 0.9 which is lower than that of Nb-2. Combining with SEM and TEM results, these results indicate that Li$^+$ insertion/extraction kinetics in Nb-2 monodisperse nanoparticles is more efficient than that in Nb-1.5 continuous mesoporous films. The continuous mesoporous Nb-0.5 films with 45 nm particle size have a b-value of 0.85, which means that the charge storage arises from both semi-infinite diffusion and capacitive processes.

The high rate capability of T-Nb$_2$O$_5$ implies that the crystal structure allows exceptionally rapid ionic and electronic transportation. This result suggests that the intercalation induced pseudocapacitance and rate ability of T-Nb$_2$O$_5$ strongly depend on the specific surface area and particle size, rather than the continuous mesoporous film structure.

The durability of the materials was assessed by cyclic testing at current densities of 0.5 A g^{-1} and 5 A g^{-1}, and the results are shown in Fig. 4c and d. The capacitance results have a slight attenuation after 300 cycles at 0.5 A g^{-1} (Fig. 4c), which represents a highly reversible Li$^+$ insertion/extraction into/from T-Nb$_2$O$_5$ enabled by the highly crystalline T-Nb$_2$O$_5$. At 0.5 A g^{-1}, Nb-2 shows an initial capacity of 528 C g^{-1}, with low capacity fading ~5.5% (499 C g^{-1}) at the end of the 300th cycle. At 5 A g^{-1}, Nb-2 still shows the highest initial capacity of 451 C g^{-1} and 380 C g^{-1} at the end of the 1000th cycle, which is ~25% more than that of Nb-1.5 and 250% of that for Nb-0.5.

Conclusions

We fabricated T-Nb$_2$O$_5$ nanomaterials through the evaporation induced self-assembly (EISA) method; two different morphologies have been achieved as monodisperse and continuous mesoporous nanofilms, which can be controllably formed by changing the addition of a triblock copolymer – F127. With this configurable microstructure, excellent electrochemical performances were achieved as a result of the unique orthorhombic crystal structure in our Nb-2 materials. For the optimized Nb-2 with a monodisperse structure and 20 nm particle size, electrochemical results show faster Li^+ intercalation kinetics, good high-rate capability with a capacity of 250 C g^{-1} at 20 A g^{-1}, and excellent cycling performance in which the specific capacity is from 528 to 499 C g^{-1} after 300 cycles at 0.5 A g^{-1} and from 451 to 380 C g^{-1} after 1000 cycles at 5 A g^{-1}. We anticipate that the discovery of this new structure–property relationship in T-Nb_2O_5 nanomaterials will shed light on novel high performance EES.

Experimental section

Materials synthesis

The orthorhombic T-Nb_2O_5 crystallite was synthesized through the evaporation induced self-assembly (EISA) process. Briefly, 1.2 g $NbCl_5$ powder (Sigma-Aldrich) was dissolved in 20 mL dry ethanol immersed in an ice bath, and a certain amount of F127 (Sigma-Aldrich) was dissolved in another 20 ml ethanol with 0.5 mL deionized water. Once these solutions are uniformly mixed, $NbCl_5$ alcohol solution was then added dropwise into the F127 solution. The mixed solution was stirred in an ice bath for 1 h in order to prevent uncontrolled hydrolysis. The homogeneous mixture was then slowly poured into Petri dishes. After slow evaporation at room temperature for 24 h, the precursor Nb/F127 films were obtained. Finally, the precursor films were thermo-annealed at 600 °C for 2 h at room temperature to obtain Nb_2O_5 nanocrystals with an orthorhombic structure.

Materials characterization

The crystalline structure was characterized by powder X-ray diffraction (XRD) at 40 kV and 100 mA with Cu Kα radiation (λ = 1.5406 Å). The morphology was observed by scanning electron microscopy (SEM, FEI-300) and transmission electron microscopy (TEM, JEOL 2100F). The amount of F127 in the samples was confirmed by thermogravimetric analysis (TGA). The specific surface area and pore structure of samples were determined by N_2 adsorption–desorption isotherms at 77 K after being degassed under vacuum at 433 K for 6 h. The Brunauer–Emmett–Teller (BET) method was utilized to calculate the specific surface areas. The total pore volume was calculated using a single point. The pore size distributions were derived from the desorption branch using the Barrett–Joyner–Halenda (BJH) model.

Electrochemical measurements

Nb_2O_5 electrodes were prepared by mixing the active material, carbon black (Timcal Super C65) and the polyvinylidene fluoride (PVdF) binder in an 8 : 1 : 1 weight ratio in *N*-methyl-2-pyrrolidinone (NMP). The homogeneous slurry was then coated onto 20 μm Cu current collectors. After drying at 100 °C for 12 hours, coated composite electrodes were pressed into 12 mm diameter using a stainless steel roller. Electrochemical tests were performed using a three-electrode system with the obtained material as the working electrode, lithium foil as the reference electrode, commercial activated carbon (Maxsorb II) as the counter electrode, the Celgard 2400 microporous film as the separator, and 1 M $LiPF_6$ (EC/DMC/DEC = 1 : 1 : 1 in volume ratio) as the electrolyte. A potential window of 1.2–3 V was chosen in this work, to investigate the electrochemical performance induced by Li-ion intercalation, since no redox peaks were found in the range of 0.8–1.2 V (*vs.* Li^+/Li) in our background tests. All electrochemical tests were performed at room temperature. Both the current density and specific capacitance were calculated based on the weight of active Nb_2O_5.

Conflicts of interest

There are no conflicts to declare.

Acknowledgements

This work was financially supported by the National Science Foundation of China (No. 51636006), the Shanghai Rising Star Program (15QA1401300) and the Engineering and Physical Sciences Research Council (EPSRC) grants-EP/N007921/1 and EP/P026435/1.

References

1 P. Simon and Y. Gogotsi, *Nat. Mater.*, 2008, **7**, 845–854.
2 P. Simon, Y. Gogotsi and B. Dunn, *Science*, 2014, **343**, 1210–1211.
3 V. Augustyn, J. Come, M. A. Lowe, J. W. Kim, P. L. Taberna, S. H. Tolbert, H. D. Abruña, P. Simon and B. Dunn, *Nat. Mater.*, 2013, **12**, 518–522.
4 Y. Jiang, M. Hu, D. Zhang, T. Yuan, W. Sun, B. Xu and M. Yan, *Nano Energy*, 2014, **5**, 60–66.
5 B. E. Conway and W. G. Pell, *J. Solid State Electrochem.*, 2003, **7**, 637–644.
6 B. E. Conway, *J. Electrochem. Soc.*, 1991, **138**, 1539–1548.
7 A. S. Arico, P. Bruce, B. Scrosati, J. M. Tarascon and W. V. Schalkwijk, *Nat. Mater.*, 2005, **4**, 366–377.
8 P. Poizot, S. Laruelle, S. Grugeon, L. Dupont and J. M. Tarascon, *Nature*, 2000, **407**, 496–499.
9 X. L. Wang, G. Li, Z. Chen, V. Augustyn, X. M. Ma, G. Wang, B. Dunn and Y. F. Lu, *Adv. Energy Mater.*, 2011, **1**, 1089–1093.
10 L. F. Nazar, G. Goward, F. Leroux, M. Duncan, H. Huang, T. Kerr and J. Gaubicher, *Int. J. Inorg. Mater.*, 2001, **3**, 191–200.
11 V. Augustyn, P. Simon and B. Dunn, *Energy Environ. Sci.*, 2014, **7**, 1597–1614.
12 T. Yuan, Y. Jiang, W. Sun, B. Xiang, Y. Li, M. Yan, B. Xu and S. Dou, *Adv. Funct. Mater.*, 2016, **26**, 2198–2206.
13 Y. Jiang, Y. Li, W. Sun, W. Huang, J. B. Liu, B. Xu, C. Jin, T. Ma, C. Wu and M. Yan, *Energy Environ. Sci.*, 2015, **8**, 1471–1479.

14 A. A. Lubimtsev, P. R. C. Kent, B. G. Sumpter and P. Ganesh, *J. Mater. Chem. A*, 2013, **1**, 14951–14956.

15 L. Kong, C. Zhang, S. Zhang, J. Wang, R. Cai, C. Lv, W. Qiao, L. Ling and D. Long, *J. Mater. Chem. A*, 2014, **2**, 17962–17970.

16 J. W. Kim, V. Augustyn and B. Dunn, *Adv. Energy Mater.*, 2012, **2**, 141–148.

17 J. Come, V. Augustyn, J. Woung Kim, P. Rozier, P. L. Taberna, P. Gogotsi, J. W. Long, B. Dunn and P. Simon, *J. Electrochem. Soc.*, 2014, **161**, A718–A725.

18 L. Kong, C. Zhang, J. Wang, W. Qiao, L. Ling and D. Long, *ACS Nano*, 2015, **9**, 11200–11208.

19 C. H. Lai, D. Ashby, M. Moz, Y. Gogotsi, L. Pilon and B. Dunn, *Langmuir*, 2017, **33**, 9407–9415.

20 L. Kong, C. Zhang, J. Wang, W. Qiao, L. Ling and D. Long, *Sci. Rep.*, 2016, **6**, 1–10.

21 J. Zhang, H. Chen, X. Sun, X. Kang, Y. Zhang, C. Xu and Y. Zhang, *J. Electrochem. Soc.*, 2017, **164**, A820–A825.

22 L. Kong, X. Cao, J. Wang, W. Qiao, L. Ling and D. Long, *J. Power Sources*, 2016, **309**, 42–49.

23 X. Liu, X. Wu and K. Scoot, *Catal. Sci. Technol.*, 2014, **4**, 3891–3898.

24 K. Brezesinski, J. Wang, J. Haetge, C. Reitz, S. O. Steinmueller, S. H. Tolbert, B. M. Smarsly, B. Dunn and T. Brezesinski, *J. Am. Chem. Soc.*, 2010, **132**, 6982–6990.

25 M. Liu, C. Yan and Y. Zhang, *Sci. Rep.*, 2015, **5**, 8326.

26 M. Wei, K. Wei, M. Lchihara and H. Zhou, *Electrochem. Commun.*, 2008, **10**, 980–983.